

High responsivity photodetectors based on graphene/WSe_2 heterostructure by photogating effect

Shuping Li(李淑萍), Ting Lei(雷挺), Zhongxing Yan(严仲兴), Yan Wang(王燕), Like Zhang(张黎可), Huayao Tu(涂华垚), Wenhua Shi(时文华), and Zhongming Zeng(曾中明)

Citation: Chin. Phys. B, 2024, 33 (**1**): 018501. DOI: 10.1088/1674-1056/acfa84
Journal homepage: http://cpb.iphy.ac.cn; http://iopscience.iop.org/cpb

What follows is a list of articles you may be interested in

Investigation of Ga_2O_3/diamond heterostructure solar-blind avalanche photodiode via TCAD simulation

Dun-Zhou Xu(许敦洲), Peng Jin(金鹏), Peng-Fei Xu(徐鹏飞), Meng-Yang Feng(冯梦阳), Ju Wu(吴巨), and Zhan-Guo Wang(王占国)
Chin. Phys. B, 2023, 32 (**10**): 108504. DOI: 10.1088/1674-1056/acc44d

Ultra-high photoresponsive photodetector based on ReS_2/SnS_2 heterostructure

Binghui Wang(王冰辉), Yanhui Xing(邢艳辉), Shengyuan Dong(董晟园), Jiahao Li(李嘉豪), Jun Han(韩军), Huayao Tu(涂华垚), Ting Lei(雷挺), Wenxin He(贺雯馨), Baoshun Zhang(张宝顺), and Zhongming Zeng(曾中明)
Chin. Phys. B, 2023, 32 (**9**): 098504. DOI: 10.1088/1674-1056/acd9c0

A field-effect WSe_2/Si heterojunction diode

Rui Yu(余睿), Zhe Sheng(盛喆), Wennan Hu(胡文楠), Yue Wang(王越), Jianguo Dong(董建国), Haoran Sun(孙浩然), Zengguang Cheng(程增光), and Zengxing Zhang(张增星)
Chin. Phys. B, 2023, 32 (**1**): 018505. DOI: 10.1088/1674-1056/ac9049

MoS_2/Si tunnel diodes based on comprehensive transfer technique

Yi Zhu(朱翊), Hongliang Lv(吕红亮), Yuming Zhang(张玉明), Ziji Jia(贾紫骥), Jiale Sun(孙佳乐), Zhijun Lyu(吕智军), and Bin Lu(芦宾)
Chin. Phys. B, 2023, 32 (**1**): 018501. DOI: 10.1088/1674-1056/ac9604

Effect of electrical contact on performance of WSe_2 field effect transistors

Yi-Di Pang(庞奕荻), En-Xiu Wu(武恩秀), Zhi-Hao Xu(徐志昊), Xiao-Dong Hu(胡晓东), Sen Wu(吴森), Lin-Yan Xu(徐临燕), and Jing Liu(刘晶)
Chin. Phys. B, 2021, 30 (**6**): 068501. DOI: 10.1088/1674-1056/abd752

High responsivity photodetectors based on graphene/WSe_2 heterostructure by photogating effect

Shuping Li(李淑萍)[1,†], Ting Lei(雷挺)[2,3,†], Zhongxing Yan(严仲兴)[1], Yan Wang(王燕)[1], Like Zhang(张黎可)[4], Huayao Tu(涂华垚)[2,3], Wenhua Shi(时文华)[2,3,‡], and Zhongming Zeng(曾中明)[2,3,§]

[1] *Suzhou Industrial Park Institute of Services Outsourcing, Suzhou* 215123, *China*
[2] *Nanofabrication Facility, Suzhou Institute of Nano-Tech and Nano-Bionics, Chinese Academy of Sciences, Suzhou* 215123, *China*
[3] *School of Nano Technology and Nano Bionics, University of Science and Technology of China, Hefei* 230026, *China*
[4] *School of Electronics and Information Engineering, Wuxi University, Wuxi* 214105, *China*

(Received 26 June 2023; revised manuscript received 15 August 2023; accepted manuscript online 18 September 2023)

Graphene, with its zero-bandgap electronic structure, is a highly promising ultra-broadband light absorbing material. However, the performance of graphene-based photodetectors is limited by weak absorption efficiency and rapid recombination of photoexcited carriers, leading to poor photodetection performance. Here, inspired by the photogating effect, we demonstrated a highly sensitive photodetector based on graphene/WSe_2 vertical heterostructure where the WSe_2 layer acts as both the light absorption layer and the localized grating layer. The graphene conductive channel is induced to produce more carriers by capacitive coupling. Due to the strong light absorption and high external quantum efficiency of multilayer WSe_2, as well as the high carrier mobility of graphene, a high photocurrent is generated in the vertical heterostructure. As a result, the photodetector exhibits ultra-high responsivity of 3.85×10^4 A/W and external quantum efficiency of 1.3×10^7%. This finding demonstrates that photogating structures can effectively enhance the sensitivity of graphene-based photodetectors and may have great potential applications in future optoelectronic devices.

Keywords: WSe_2, heterostructure, photodetector, photogating effect

PACS: 85.60.–q, 85.60.Gz, 73.40.Lq **DOI:** 10.1088/1674-1056/acfa84

1. Introduction

Photodetectors based on transition metal dichalcogenides (TMDCs) such as MoS_2 and WSe_2 have received much attention due to their flexible structure,[1,2] tunable bandgap,[3,4] and high absorption coefficient.[5,6] Previous studies have demonstrated that the photodetection efficiency of monolayer MoS_2 and WSe_2 photodetectors is as low as a few hundred mA/W, due to the light absorption limitations and the effects of non-optimal contact at the metal electrode and material interface.[7,8] Therefore, to obtain high-performance photodetectors, many researchers have turned to heterostructures based on graphene/TMDCs to prepare low-resistance devices.[9–11] Moreover, graphene-based heterostructures retain the inherent photoelectronic properties of a single material due to weak van der Waals forces between layers and the lack of surface dangling bonds, which can further improve device performance.[12–15] For example, Tan *et al.* and Yeh *et al.* reported that the photodetection efficiency of WSe_2 and WS_2 photodetectors increased to 350 A/W and 3.5 A/W, respectively, by using graphene as a transparent contact electrode.[16,17]

The tungsten disulfide (WSe_2) has a tunable bandgap (1.2 eV–1.67 eV), bipolar transport behavior, and excellent photoelectronic properties, and has been widely studied as a potential candidate for next-generation optoelectronic devices, such as solar cells, photodetectors, and photonic modulators.[18–21] In addition, graphene can achieve wideband photodetection from ultraviolet to terahertz wavelengths due to its unique zero bandgap structure.[22,23] Furthermore, graphene-based photodetectors exhibit super-fast response speeds due to their ultra-high carrier mobility.[24] Unfortunately, the light absorption efficiency of monolayer graphene is only about 2.3% and usually lacks high photoresponsivity.[25] To generate higher photocurrent, it is possible to construct an internal electric field to separate photo-generated electron–hole pairs, thereby extending the carrier lifetime.[10,26] Therefore, by fabricating a vertical heterostructure device and combining the advantages of WSe_2 and graphene, it is promising to improve the overall performance of the photodetector.

In the present research, we fabricated a high photodetection efficiency photodetector based on a graphene/WSe_2 vertical heterostructure. The device covered a layer of high light-absorbing WSe_2 material on the graphene channel, which significantly enhanced the device's light absorption. At the same

[†]These authors contributed equally to this work.
[‡]Corresponding author. E-mail: whshi2007@sinano.ac.cn
[§]Corresponding author. E-mail: zmzeng2012@sinano.ac.cn

© 2024 Chinese Physical Society and IOP Publishing Ltd

time, we used the localized grating layer formed by the WSe_2 material to regulate the carrier concentration of the underlying graphene. At room temperature, the external quantum efficiency of the device reached 1.3×10^7%, and the photodetection efficiency reached 3.85×10^4 A/W, which is 2–3 orders of magnitude higher than that of the WSe_2 photodetector. These results demonstrate that using WSe_2 material as the localized grating layer is an effective way to achieve high photoresponsivity and high external quantum efficiency.

2. Experimental details

2.1. Device fabrication

The graphene/WSe_2 vdW heterostructure was fabricated using mechanical exfoliation technique. First, few layers graphene flake was exfoliated using 3M tape. Next, the graphene device was fabricated using layout design software (L-edit), electron beam lithography, and electron beam evaporation processes. Finally, WSe_2 thin film material is obtained through mechanical exfoliation and transferred onto the previously fabricated graphene device, resulting in the graphene/WSe_2vertical device.

2.2. Device characterization

The morphology and thickness of the graphene/WSe_2 vdW heterostructure were measured using an atomic force microscope (AFM). The quality of the heterostructure device was characterized using a Raman spectrometer with a laser wavelength of 532 nm. The photoelectric performance was measured using a semiconductor parameter analyzer (Keithley 2400 and 2612B) in a dark room at room temperature and a laser source with a tunable wavelength of 365 nm–965 nm.

3. Results and discussion

3.1. Device structure and microscopic characterization

Figure 1(a) shows a schematic diagram of the graphene/WSe_2 vertical heterostructure device on an Si/SiO_2 substrate. The device is obtained by mechanically exfoliating WSe_2 thin film material and transferring it onto a previously fabricated graphene device. Figure 1(b) shows an optical image of the graphene/WSe_2 heterostructure, where WSe_2 is used as the light-absorbing layer and the localized grating layer, and graphene as the conductive channel layer. The built-in electric field between graphene and WSe_2 can enhance the separation of electron–hole pairs and reduce the recombination probability. The morphology and thickness of the heterostructure device were characterized by atomic force microscopy (AFM). Figure 1(c) shows the AFM image of the graphene/WSe_2 vertical heterostructure device, where the orange dashed line represents WSe_2, the red dashed line represents graphene, and the scale bar is 10 μm. The thickness information of the graphene/WSe_2 heterostructure device was extracted from the inset, where the thicknesses of WSe_2 and graphene were 11 nm and 7 nm, respectively.

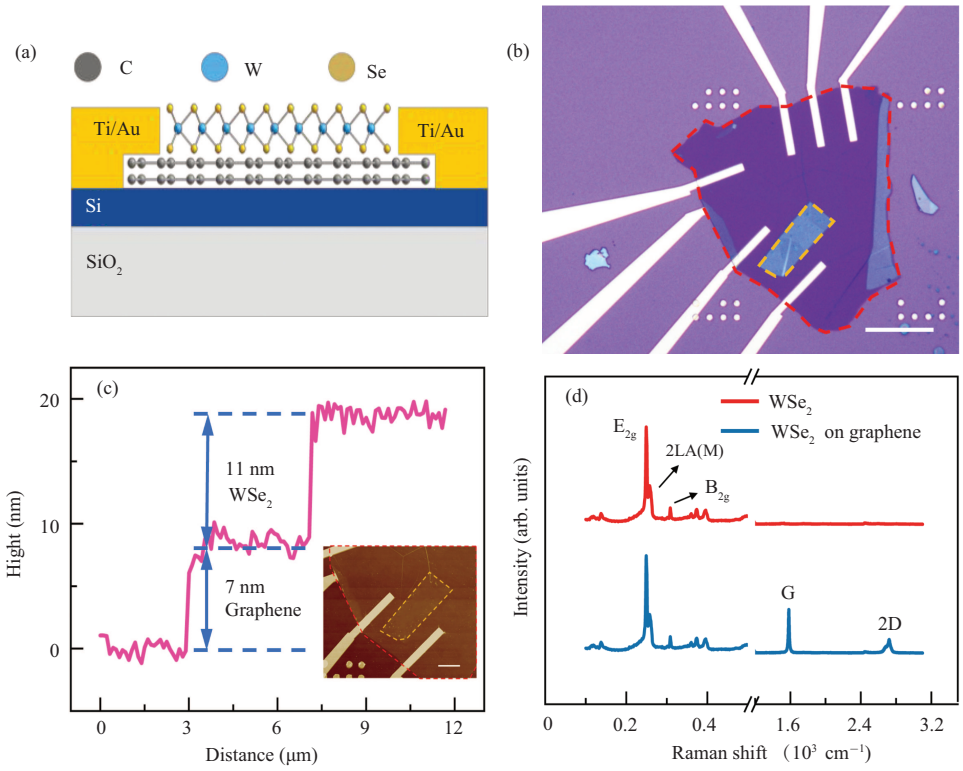


Fig. 1. (a) Schematic structure of graphene/WSe_2 photodetector; (b) optical microscopy image of the graphene/WSe_2 heterostructure (red line is the lower graphene layer, orange line is the upper WSe_2 layer), scale bar: 10 μm; (c) thickness of heterostructure device extracted from AFM image (the thickness of graphene (WSe_2) was 7 nm (11 nm)), the inset is AFM image, scale bar: 5 μm; (d) Raman spectra of individual WSe_2 and the graphene/WSe_2 heterostructure region.

Figure 1(d) shows the Raman spectroscopy characterization results of the WSe_2 and the graphene/WSe_2 heterostructure region. For the pristine WSe_2 material, the Raman spectrum exhibits three prominent peaks: E_{2g} at 249 cm^{-1}, 2LA(M) at 257 cm^{-1}, and B_{2g} at 308 cm^{-1}, respectively. The Raman spectrum of the graphene/WSe_2 heterostructure region shows an additional characteristic peak of graphene at 1582.5 cm^{-1}. This G peak originates from the E_{2g} phonon mode, and the two-dimensional (2D) vibration mode's characteristic peak is located at 2715.6 cm^{-1}, corresponding to double phonon resonance. In the heterostructure region, the signal peak of graphene is much weaker than the Raman intensity of the WSe_2 material, due to the fact that the WSe_2 material is covered on top of graphene, causing it to receive much less Raman laser power.

3.2. Electrical characterizations of the graphene/WSe_2 heterostructure device

Figures 2(a) and 2(b) show the output characteristics of the WSe_2/h-BN heterostructure device at different gate voltages (V_g). As the V_g increases from 0 V to 50 V, the source–drain current (I_{ds}) also increases, and the output characteristics exhibit a sub-linear behavior due to the Fermi level pinning effect between the metal electrode and the thin film material, as shown in the logarithmic coordinate plot in Fig. S1. As the V_g varies from −60 V to −10 V, the overall magnitude of the I_{ds} increases with the increase of the V_g, corresponding to the transfer characteristic curve shown in Fig. S2, indicating that the WSe_2/h-BN heterostructure device exhibits bipolar semiconductor characteristics. The electric field mobility (μ_{FE}) of the WSe_2/h-BN heterostructure device is calculated using the following formula:

$$\mu = g_m \frac{L}{W} \cdot \frac{1}{C_i} \cdot \frac{1}{V_{ds}}, \tag{1}$$

$$C_i = C_{h-BN} \cdot C_{SiO_2} / \left(C_{h-BN} + C_{SiO_2}\right), \tag{2}$$

where μ is the mobility of the device, L is the channel length (5.4 μm), W is the channel width (8.3 μm), ε represents the vacuum permittivity (8.854×10^{12} F/m), ε_r represents the relative permittivity of the material (3.9 for SiO_2 and 3.5 for h-BN), and d represents the thickness of SiO_2 (300 nm). Based on Eqs. (1) and (2), the electron (hole) mobility of the WSe_2/h-BN heterostructure device at a source–drain voltage (V_{ds}) of 1 V can be calculated as 7.20 $cm^2 \cdot V^{-1} \cdot s^{-1}$ (25.17 $cm^2 \cdot V^{-1} \cdot s^{-1}$).

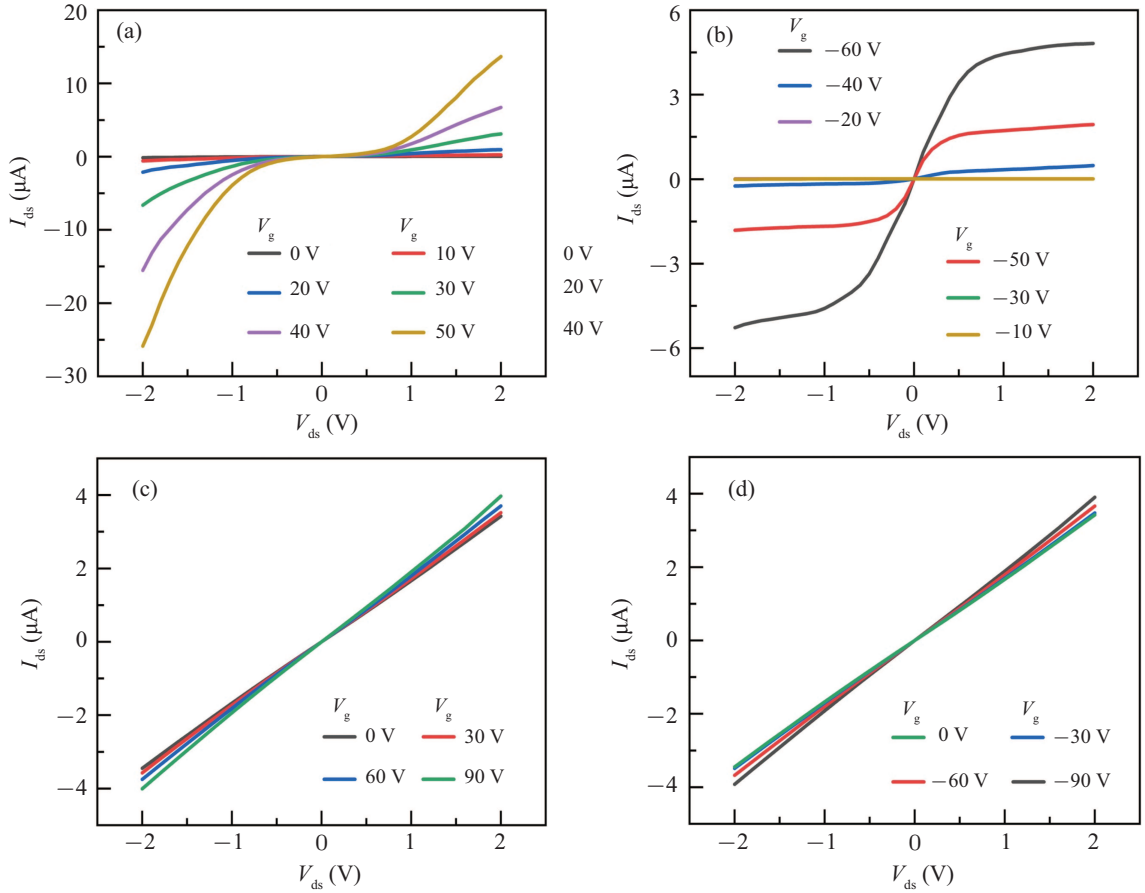


Fig. 2. Electrical characteristics of WSe_2/h-BN heterostructure device and graphene/WSe_2 heterostructure device under dark conditions. (a) Output characteristic curve of WSe_2/h-BN heterostructure device with gate voltage ranging from 0 V to 50 V; (b) output characteristic curve with gate voltage ranging from −60 V to −10 V; (c) output characteristic curve of graphene/WSe_2 heterostructure device with gate voltage ranging from 0 V to 90 V; (d) output characteristic curve with gate voltage ranging from −90 V to 0 V.

Figures 2(c) and 2(d) show the output characteristics of the heterostructure device as the V_g varies from 0 V to 90 V and from −90 V to 0 V, respectively. The results indicate Ohmic contact between graphene and the metal electrode without a Schottky barrier. The concentration of graphene conductive channel can be controlled by the V_g. As the V_g increases from 0 V to 90 V, the I_{ds} increases. Conversely, as the V_g increases from −90 V to 0 V, the I_{ds} decreases. This is consistent with the transfer characteristics curve shown in Fig. S3, demonstrating the bipolar semiconductor behavior of the heterostructure device.

Based on the above outstanding electrical performance, we further investigated the photodetection performance of WSe_2/h-BN heterostructure devices. Figure 3(a) shows the output characteristics of the heterostructure device under visible light irradiation at 532 nm, with P_{in} values ranging from 1.39 mW/cm^2 to 10.12 mW/cm^2. As can be seen, the heterostructure device exhibits a large photocurrent at various light power densities, and the photocurrent increases with increasing P_{in} values. When P_{in} is 10.12 mW/cm^2, the I_{ds} can reach 5.74×10^{-6} A, which is more than 5 μA higher than that under dark conditions. Figure 3(b) shows the dependence of the responsivity of the heterostructure device on the V_{ds} and the incident light power density. The results show that R sharply increases with increasing the V_{ds}, and reaches a maximum value of 1535.05 A/W at $P_{in} = 2.71$ mW/cm^2 and $V_{ds} = 2$ V. Figures 3(c) and 3(d) show the incident light power distribution curves of the R and D^* of the heterostructure device, demonstrating good response characteristics of the WSe_2/h-BN heterostructure device at various light power densities. Among them, when P_{in} is 1.39 mW/cm^2 and the I_{ds} is 1 V, the R and D^* can reach the highest values, which are 295.12 A/W and 4.19×10^9 Jones, respectively.

Next, we will delve into the photogating effect in the graphene/WSe_2 vertical heterostructure device and its origin, as shown in Fig. 4(a). Taking the example of the graphene/WSe_2 vertical heterostructure device operating at a gate voltage of $V_g < 0$ V, when WSe_2 and graphene come into contact with each other, due to the difference in carrier concentration and Fermi level, the holes in WSe_2 will diffuse towards graphene under the effect of carrier concentration gradient. Finally, under no external voltage, the diffusion and drift motions of the charge carriers are balanced, achieving dynamic equilibrium. In this state, an intrinsic electric field pointing from WSe_2 to graphene is generated in the depletion layer formed between them. By changing the external voltage, the width of the depletion layer and the strength of the intrinsic electric field can be further adjusted, thereby achieving the tuning of the heterostructure device's performance.

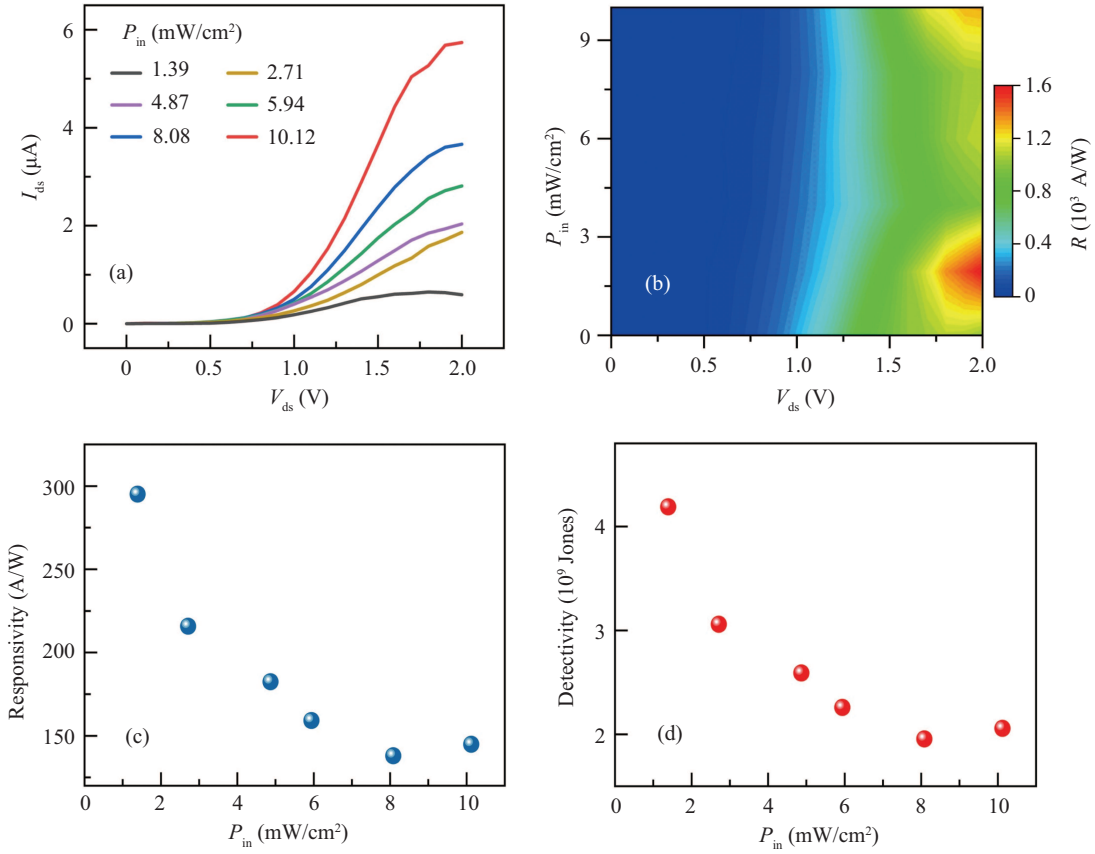


Fig. 3. WSe_2/h-BN heterostructure device: (a) output characteristic curves under different incident light intensities in dark conditions (wavelength λ = 532 nm, $V_g = 0$ V); (b) the 2D relationship between photoresponsivity and incident light power density and source–drain voltage ($\lambda = 532$ nm, $V_g = 0$ V); the variation of (c) photoresponsivity and (d) specific detectivity with incident light power density.

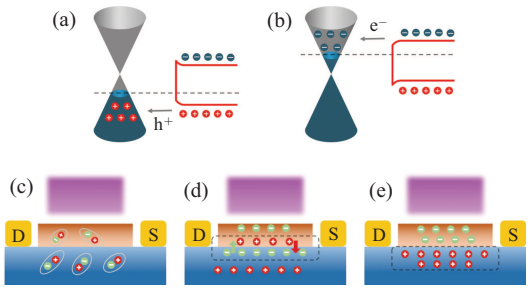


Fig. 4. Graphene/WSe_2 vertical heterostructure device. Energy band diagrams of graphene/WSe_2 vertical heterostructure devices under different gate voltages: (a) $V_g < 0$ V and (b) $V_g > 0$ V (with fixed incident wavelength of 365 nm, red represents holes and dark blue represents electrons); the schematic diagrams of (c) generation, (d) transfer, and (e) confinement of photoexcited electron–hole pairs. The upper layer is made of WSe_2 material, the lower layer is made of graphene material, green circles represent electrons, red circles represent holes.

Under dark conditions, the majority of the I_{ds} in heterostructure devices comes from holes in graphene. When a 365-nm wavelength laser is irradiated on the heterostructure device, photo-generated electron–hole pairs are excited in both WSe_2 and graphene materials, as shown in Fig. 4(c). Due to the formation of a built-in electric field from graphene to WSe_2 at the interface, the photogenerated electron–hole pairs are separated and move towards each material under the influence of the built-in electric field. Specifically, the holes in WSe_2 are transferred to the underlying graphene layer, while the photogenerated electrons in graphene are transferred to the upper WSe_2 layer, as shown in Fig. 4(d). This process increases the hole concentration in the graphene conductive channel, and the holes drift under the influence of the V_{ds}, contributing to the increment of the photocurrent. In addition, due to the existence of the built-in electric field in the heterostructure device, the electrons transferred from graphene are confined to the WSe_2 layer, as shown in Fig. 4(e). This confinement of electrons in the WSe_2 layer produces a modulation effect similar to the gate voltage. Under this strong coupling effect, electrons in the WSe_2 layer induce more holes to be generated in the graphene layer, thereby increasing the carrier concentration in the channel and improving the photo-detection performance of the heterostructure device by an order of magnitude.

Based on the research of the electrical characteristics of heterostructure devices and the photoelectric properties of WSe_2 transistors, we continued to test the photo-detection performance of graphene/WSe_2 heterostructure devices under different conditions. When the V_g was 0 V, we tested the output characteristic curve of the heterostructure device under dark conditions and 365-nm incident wavelength light illumination, as shown in Fig. 5(a). With the increase of the V_{ds}, the photoelectric current of the heterostructure device also increased, indicating that the collection efficiency of photo-generated carriers gradually improved. At the same time, we also tested the transfer characteristic curve of the heterostructure device under dark conditions and 365-nm incident wavelength light illumination with a fixed V_{ds} of 1 V, as shown in Fig. 5(b). It can be seen that the photoelectric current of the heterostructure device under the V_g regulation shows a trend of decreasing first and then increasing, indicating that the heterostructure device has bipolar semiconductor characteristics consistent with the experimental results under dark conditions.

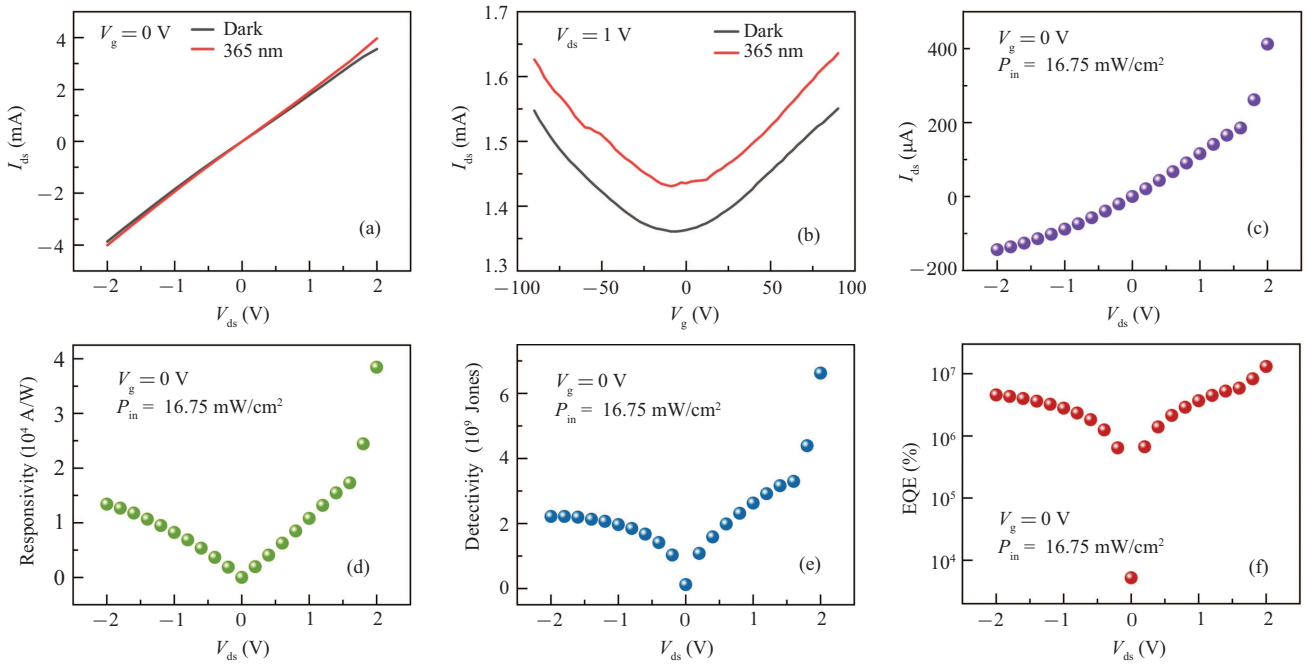


Fig. 5. Graphene/WSe_2 vertical heterostructure device: (a) output characteristics under dark and 365-nm wavelength light illumination ($V_g = 0$ V); (b) transfer characteristics under dark ($V_{ds} = 1$ V); (c) extracted photocurrent as a function of V_{ds} ($V_g = 0$ V, $\lambda = 365$ nm); (d) the relationship between responsivity R, (e) detectivity D^*, and (f) external quantum efficiency (EQE) with V_{ds}.

Figures 5(d) and 5(e) show the curves of R and D^* of the graphene/WSe_2 vertical heterostructure device as a function of source–drain voltage (V_{ds}), respectively. The results indicate that the R and D^* values of the device also increase with the increase of V_{ds}. The R and D^* of the heterostructure device can be expressed by the following equations:[27–31]

$$R = \frac{I_{ph}}{P_{in} \cdot A}, \tag{3}$$

$$D^* = \frac{R\sqrt{A}}{\sqrt{2e \cdot I_{dark}}}, \tag{4}$$

where P_{in}, A, and e are the incident optical power density, effective illuminated area, and electron charge.

When the device is illuminated with 365-nm wavelength light at a power density of 16.75 mW/cm^2 and the source–drain voltage is 1 V, R and D^* reach 1.34×10^4 A/W and 2.21×10^9 Jones, respectively. When the source–drain voltage is further increased to 2 V, the R and D^* of the device are improved to 3.85×10^4 A/W and 6.62×10^9 Jones, respectively. In addition, to further improve the photoresponsivity of the heterostructure device, the gate voltage of the device can be increased to adjust the carrier concentration in the conductive channel. Furthermore, figure 5(f) demonstrates the variation of external quantum efficiency (EQE) with different source–drain voltages. The EQE is a dimensionless quantity that represents the ratio of collected electrons to incident photons in a device, and can be calculated using the following formula:

$$\mathrm{EQE} = \frac{R \cdot h \cdot c}{e \cdot \lambda},$$

where R is the photoresponsivity, h is the Planck constant (6.63×10^{-34} J · s), λ represents the wavelength of the incident laser, and c is the speed of light in vacuum. For the heterostructure device, the EQE reaches 4.6×10^4% at a source–drain voltage of -2 V. Continuing to increase the voltage to -2 V, the EQE increases to 1.3×10^7%, indicating that the light absorption efficiency can be improved by changing the source–drain voltage of the device. Finally, This is also comparable to those in previous works (supporting information, Table S1).

4. Conclusion

In summary, we demonstrated a graphene/WSe_2 vertical heterostructure based highly sensitive photodetector, where the WSe_2 layer plays a dual role of both the light absorption layer and the localized grating layer. The graphene conductive channel is induced to produce more charge carriers by capacitive coupling. Under the strong photogating effect, graphene/WSe_2 vertical heterostructure exhibits excellent optoelectronic properties at room temperature, with a detectivity and external quantum efficiency of 6.62×10^9 Jones and 1.3×10^7%, respectively. Furthermore, the photoresponsivity reaches 3.85×10^4 A/W, which is two to three orders of magnitude higher than that of theWSe_2 photodetector.

Acknowledgements

Project supported by the National Natural Science Foundation of China (Grant No. 11974379), the National Key Basic Research and Development Program of China (Grant No. 2021YFC2203400), and Jiangsu Vocational Education Integrated Circuit Technology "Double-Qualified" Famous Teacher Studio (Grant No. 2022-13).

References

[1] Lin P, Zhu L, Li D, Xu L, Pan C and Wang Z 2018 *Adv. Funct. Mater.* **28** 1802849
[2] He H K, Yang F F and Yang R 2020 *Phys. Chem. Chem. Phys.* **22** 20658
[3] Ross J S, Klement P, Jones A M, Ghimire N J, Yan J, Mandrus D G, Taniguchi T, Watanabe K, Kitamura K, Yao W, Cobden D H and Xu X 2014 *Nat. Nanotechnol.* **9** 268
[4] Cheng Q, Pang J, Sun D, Wang J, Zhang S, Liu F, Chen Y, Yang R, Liang N, Lu X, Ji Y, Wang J, Zhang C, Sang Y, Liu H and Zhou W 2020 *InfoMat* **2** 656
[5] Zhang J, Du L, Feng S, Zhang R W, Cao B, Zou C, Chen Y, Liao M, Zhang B and Yang S A 2019 *Nat. Commun.* **10** 4226
[6] Luo X, Andrews K, Wang T, Bowman A, Zhou Z and Xu Y Q 2019 *Nanoscale* **11** 7358
[7] Yin Z, Hai Li, Li H, Jiang L, Shi Y, Sun Y, Lu G, Zhang Q, Chen X and Zhang A H 2012 *ACS Nano* **6** 74
[8] Chu C H, Lin H C, Yeh C H, Liang Z Y, Chou M Y and Chiu P W 2019 *ACS Nano* **13** 8146
[9] Murali K, Abraham N, Das S, Kallatt S and Majumdar K 2019 *ACS Appl. Mater. & Inter.* **11** 30010
[10] Kang B, Kim Y, Yoo W J and Lee C 2018 *Small* **14** e1802593
[11] Kim H J, Lee K J, Park J, Shin G H, Park H, Yu K and Choi S Y 2020 *ACS Appl. Mater. & Inter.* **12** 38563
[12] Geim A K and Grigorieva I V 2013 *Nature* **499** 419
[13] Liu Y, Weiss N O, Duan X, Cheng H C, Huang Y and Duan X 2016 *Nat. Rev. Mater.* **1** 1
[14] Omar S, Madhushankar B N and van Wees B J 2019 *Phys. Rev. B* **100** 155415
[15] Zhang Z, Lin P, Liao Q, Kang Z, Si H and Zhang Y 2019 *Adv. Mater.* **31** e1806411
[16] Zhou Y, Tan H, Sheng Y, Fan Y, Xu W and Warner J H 2018 *ACS Nano* **12** 4669
[17] Yeh C H, Liang Z Y, Lin Y C, Wu T L, Fan T, Chu Y C, Ma C H, Liu Y C, Chu Y H, Suenaga K and Chiu P W 2017 *ACS Appl. Mater. & Inter.* **9** 36181
[18] Xing X, Zhao L, Zhang W, Wang Z, Su H, Chen H, Ma G, Dai J and Zhang W 2020 *Nanoscale* **12** 2498
[19] Tan C, Wang H, Zhu X, Gao W, Li H, Chen J, Li G, Chen L, Xu J, Hu X, Li L and Zhai T 2020 *ACS Appl. Mater. & Inter.* **12** 44934
[20] Tan C, Yin S, Chen J, Lu Y, Wei W, Du H, Liu K, Wang F, Zhai T and Li L 2021 *ACS Nano* **15** 8328
[21] Chen J, Bailey C S, Hong Y, Wang L, Cai Z, Shen L, Hou B, Wang Y, Shi H, Sambur J, Ren W, Pop E and Cronin S B 2019 *ACS Photon.* **6** 787
[22] Jiang H, Wei J, Sun F, Nie C, Fu J, Shi H, Sun J, Wei X and Qiu C W 2022 *ACS Nano* **16** 4458
[23] Zhao Y, Tsai T Y, Wu G, Ó Coileáin C, Zhao Y F, Zhang D, Hung K M, Chang C R, Wu Y R and Wu H C 2021 *ACS Appl. Mater. & Inter.* **13** 47198
[24] Wei K, Sui Y, Xu Z, Kang Y, You J, Tang Y, Li H, Ma Y, Ouyang H, Zheng X, Cheng X and Jiang T 2020 *Nat. Commun.* **11** 3876
[25] Wang Y, Ho V X, Pradhan P, Cooney M P and Vinh N Q 2021 *ACS Appl. Nano Mater.* **4** 8539
[26] Shin J and Yoo H 2023 *Nanomaterials* **13** 882
[27] Fang Y, Armin A, Meredith P and Huang J 2019 *Nat. Photon.* **13** 1
[28] Chen Y, Wang Y, Wang Z, Gu Y, Ye Y, Chai X, Ye J, Chen Y, Xie R, Zhou Y, Hu Z, Li Q, Zhang L, Wang F, Wang P, Miao J, Wang J, Chen X, Lu W, Zhou P and Hu W 2021 *Nat. Electron.* **4** 357
[29] Rogalski A 2022 *Nat. Nanotechnol.* **17** 217
[30] Wang F, Liu Z, Zhang T, Long M, Wang X, Xie R, Ge H, Wang H, Hou J and Gu Y 2022 *Adv. Mater.* **34** 2203283
[31] Wang F, Zhang T, Xie R, Wang Z and Hu W 2023 *Nat. Commun.* **14** 2224